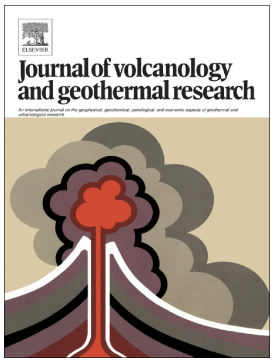

Exploring the role of fluid-solid interactions for modelling volcano deformation

Rami Alshembari, James Hickey, Ben J. Williamson, Katharine Cashman

PII: S0377-0273(22)00066-X

DOI: https://doi.org/10.1016/j.jvolgeores.2022.107535

Reference: VOLGEO 107535

To appear in: *Journal of Volcanology and Geothermal Research*

Received date: 5 November 2021

Revised date: 28 February 2022

Accepted date: 12 March 2022

Please cite this article as: R. Alshembari, J. Hickey, B.J. Williamson, et al., Exploring the role of fluid-solid interactions for modelling volcano deformation, *Journal of Volcanology and Geothermal Research* (2021), https://doi.org/10.1016/j.jvolgeores.2022.107535

Exploring the role of fluid-solid interactions for modelling volcano deformation

Rami Alshembari[1], James Hickey[1], Ben J. Williamson[1] and Katharine Cashman[2,3]

[1] Camborne School of Mines, University of Exeter, Penryn, Cornwall, TR10 9FE, UK

[2] School of Earth Sciences, University of Bristol, Wills Memorial Building, Queens Road, Clifton, BS8 1RJ, UK

[3] Department of Geological Sciences, University of Oregon, Eugene, OR 97405, USA

Corresponding author: Rami Alshembari (ra500@exeter.ac.uk)

Key Points:

- Two magma intrusion schemes are compared, examining the magma reservoir pressure evolution through time and resultant surface deformation
- Reservoir pressurization is influenced by characteristic timescales related to the dimensions of the feeder system and magma rheology

Abstract

Investigating the temporal development of magma reservoir pressure and associated surface displacements can reveal fundamental aspects of subsurface magmatic processes and aid in eruption forecasting. The limitation with existing volcano deformation models is that they typically ignore magma intrusion dynamics and focus on the response of surrounding rocks to source boundary pressure. Magma fluid dynamics should be incorporated into magmatic modelling to track the temporal development of a system, instead of the widely used kinematic techniques. Here, we compare analytical and numerical solutions for magma intrusion into a shallow reservoir, using two schemes of intrusion boundary condition, inlet pressure and inlet mass flow. Model sensitivity tests are conducted to explore key factors controlling the two-way coupling between solid and fluid components, assuming an incompressible magma for a first-order approach. For intrusions of viscous magma ($\gtrapprox 10^8$ Pa s) or a narrow feeder conduit (5-20 m), applying an inlet pressure causes the resultant pressure and surface deformation to develop at a very slow rate; lower viscosity magmas produce faster deformation rates. The mass flow boundary condition reduces the number of model parameters as it is independent of poorly constrained parameters such as conduit and magma characteristics. For both boundary conditions, reservoir pressurization, and hence spatiotemporal surface deformation, are strongly influenced by reservoir geometry due to geometric compressibility. Our results provide fundamental knowledge to advance to more complex coupled fluid-solid mechanics models in volcano geodesy.

1 Introduction

Most volcanic eruptions are preceded by a period of volcanic unrest, defined as volcanic activity above the background, or baseline, that may be cause for concern (Gottsmann et al., 2017; Phillipson et al., 2013). Volcano deformation monitoring is one of the primary techniques used to track volcanic unrest and underlying magmatic processes. Its effectiveness, however, is limited by our understanding of the mechanisms driving volcanic inflation and how these relate to potential eruptive activity (Biggs et al., 2014; Dzurisin, 2006; Fialko et al., 2001; Phillipson et al., 2013; Segall, 2013; Sparks et al., 2012).

Ground inflation can occur as magma ascends through the crust and accumulates in reservoirs if accompanied by increases in internal reservoir pressure. When magma is expelled from a reservoir, by intrusion or eruption, the internal pressure will decrease, and deflation may occur (Dzurisin, 2006; Segall, 2019). Traditionally, volcano geodetic data is interpreted using the kinematic Mogi model, which gives a solution for a pressurized point source embedded in an elastic, homogeneous, and isotropic half-space (Mogi, 1958). The introduction of the Mogi model has been followed by several analytical studies that consider finite cavity magma reservoir geometries, which are also placed in a homogeneous half-space domain (Davis, 1986; Fialko et al., 2001; McTigue, 1987; Yang et al., 1988). Although these models provide the basis for volcano deformation modelling, their accuracy is limited by assumptions of simple elastic subsurface rheology and neglect of possible viscoelastic behaviour, which results from elevated thermal regimes (Bonafede et al., 1986; Dragoni & Magnanensi, 1989; Head et al., 2019; Hickey et al., 2016; Del Negro et al., 2009; Segall, 2016). Current numerical models can account for viscoelastic crustal rheologies, but many numerical and analytical models still consider the magma reservoir (i.e., the deformation source) as a cavity. This is a first-order approximation; in nature, deformation sources are complex magmatic reservoirs that contain melt and/or crystal mush and may be connected to vertically extensive transcrustal magmatic systems (Bachmann & Huber, 2016; Jackson et al., 2018; Mutch et al., 2019). From this perspective, models of magmatic systems should also consider the dynamic interaction between solid mechanics (i.e., the crust) and fluid dynamics (i.e., the magma).

Some recent studies have attempted to couple magmatic fluid dynamics and structural mechanics, but have been applied only to particular examples of volcanic deformation data (e.g., Bato et al., 2018; Lengliné et al., 2008; Le Mével et al., 2016; Reverso et al., 2014) without fully exploring the impacts of required model parameters. In this paper we present a general view of the magma intrusion process and show the implications of different magma properties, intrusion characteristics, and contrasting boundary conditions on the resultant spatiotemporal surface deformation. We move beyond the traditional approach of modelling the deformation source as a cavity with an assigned uniform boundary load or volume change and couple solid and fluid mechanics to consider the two-way interaction between the host rock and a magma reservoir. After benchmarking the numerical solution with the analytical solution, we numerically explore the impact of different magmatic parameters, including magma viscosity, conduit geometry and

reservoir geometry on the predicted surface deformation and subsurface fluid dynamics. Our first-order numerical models and parameter sensitivity testing are designed to explore and better understand the role of fluid-solid interactions for modelling volcano deformation, such that future model improvements and applications to geodetic data are better informed of basic model dependencies.

2 Analytical solutions for magma intrusion into a fluid-filled crustal reservoir

As a first approach, we derive the evolution of pressure within a crustal magma reservoir caused by magma replenishment from a deep source through a vertical conduit. In this simplified model, we assume: i) a spherical reservoir embedded within an elastic half-space, connected to a source region via a vertical cylindrical (pipe-like) conduit, ii) that the magma in the conduit and reservoir is a single-phase fluid, and iii) that the reservoir is composed of 100% melt (Figure 1a). The inclusion of melt fractions less than 100% was beyond the scope of our current study, but the applicability and limitations of our approach, and suggestions for improvements, are discussed later. We consider two schemes of magma intrusion from the source: firstly, a defined pressure that drives fluid flow, and secondly a defined inlet mass flow rate. In both cases, we investigate a piecewise function for inlet pressure or inlet volumetric flow at the conduit base (Figure 1b). This approach will highlight the influence of different inlet boundary conditions on the temporal evolution of reservoir overpressure and surface deformation. The inlet pressure approach builds on the work of Le Mével et al. (2016), extending the solution to a more general function of inlet pressure; the inlet mass flow rate derivation is presented for the first time. A spherical reservoir is considered for simplicity; elliptical magma reservoir geometries are addressed numerically in section 4.

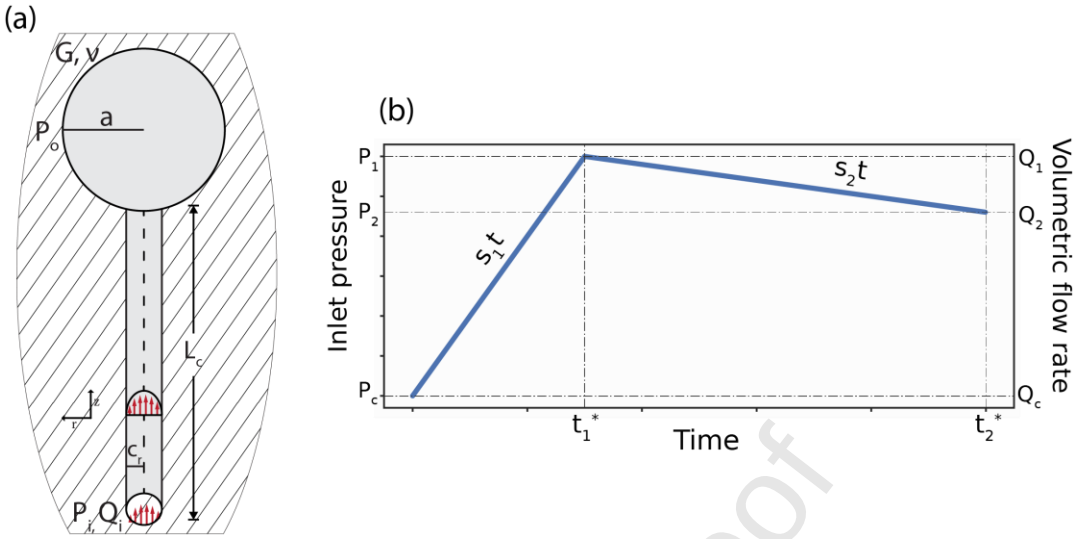

Figure 1. *(a) Illustration of the analytical model in an axisymmetric 2D geometry. A shallow magma reservoir of radius a is connected to a vertical cylindrical conduit of radius c_r and length L_c, surrounded by an elastic host rock of shear modulus G and Poisson's ratio ν. The pressure in the reservoir P_o develops due to fluid intrusion at the base which has a driving pressure P_i. (b) The inlet pressure or volumetric flow rate, applied at the conduit base. The inlet pressure or mass flow is a piecewise function of two periods with different development rates, s_1 and s_2.*

2.1 Governing equations

When melt flows through a vertical cylindrical conduit (Figure 1a), the internal roughness of the conduit wall will resist the flow due to the no-slip velocity condition of the conduit walls. The velocity of the fluid flow is maximum at the centre of the pipe and decreases towards the wall. The Reynolds number (Re) is a dimensionless quantity used to classify whether the flow will be laminar or turbulent. For fully developed flow in pipes with a circular cross-section, Reynolds number, Re, is defined as:

$$\mathrm{Re} = \frac{2\rho_m \mathrm{Q_i}}{\pi c_r \eta_m} \qquad (1)$$

where c_r is the pipe radius, $\mathrm{Q_i}$ is the volume flow rate, ρ_m is the fluid density, and η_m is the fluid viscosity (Turcotte & Schubert, 2014). The flow is laminar as long as the Reynolds number lies below the critical Reynolds number $Re_{crit} \sim 2000$ (Palacios & Armstrong, 1965). The maximum possible value of Re is ~ 0.2 when using average flow values of $\rho_m <$

$2600\ \mathrm{kg\ m^{-3}}$, $\eta_m > 10^4\ \mathrm{Pa\ s}$, $c_r > 10\ \mathrm{m}$ and $Q < 10\ m^3 s^{-1}$ (Le Mével et al., 2016). Therefore, for our application, the melt flows in a fully laminar regime.

The flow rate through a cylindrical conduit of radius c_r and length L_c is given by the Hagen-Poiseuille law (Jaupart & Tait, 1990):

$$Q = \frac{\dot{m}}{\rho_m} = -\frac{\pi c_r^4}{8\eta_m}\left(\frac{dP}{dz} + \rho_m g\right) \quad 2)$$

where $\dot{m}$ is the mass flux, Q is the volumetric flow, P is the pressure, z is the vertical coordinate and g is the gravitational acceleration (see Supplementary Material for derivation).

Considering a constant-pressure reduction through the conduit length L_c, the pressure variation in the vertical direction is given by:

$$\frac{dP}{dz} = \frac{P_i - P_o}{L_c} \quad 3)$$

where P_i and P_o are the pressure at the conduit base and the pressure at the reservoir entrance, respectively (Figure 1a). The pressure at any point equals the sum of the lithostatic pressure and pressure induced by the mass flow:

$$P_i = (d + a + L_c)\,\rho_r g + \Delta P_i \quad 4)$$

$$P_o = (d + a)\,\rho_r g + \Delta P_o \quad 5)$$

where d, a and ρ_r are the magma reservoir central depth, reservoir radius and crustal rock density, respectively, and ΔP_i, ΔP_o are the inlet and outlet pressure change due to the flow. Substituting equations (4) & (5) into (3) gives:

$$\frac{dP}{dz} = \frac{P_i - P_o}{L_c} = \frac{\Delta P_o - \Delta P_i - \rho_r g L_c}{L_c} \quad 6)$$

The equation for volumetric flow is provided by substituting equation (6) into equation (2):

$$Q = \frac{\pi c_r^4}{8\eta_m L_c}\left(\Delta P_i - \Delta P_o + (\rho_r - \rho_m) g L_c\right) \quad 7)$$

Conduit flow is driven primarily by the pressure difference between the conduit base and reservoir entrance. The volumetric flow rate is directly proportional to c_r^4 and hence is highly sensitive to the conduit dimensions.

The reservoir volume change is driven by the pressure change, which is mainly a function of magma and chamber compressibility:

$$\Delta V = \Delta P V_0(\beta_m + \beta_w) \quad \rightarrow \quad \Delta P = \frac{\Delta V}{V_0(\beta_m + \beta_w)} \quad 8)$$

where ΔV, ΔP, V_0 are the volume change, pressure change and the initial volume of the reservoir, respectively and β_m and β_w are the magma and wall rock compressibility (Anderson & Segall, 2011). Here, we assume the magma to be fully incompressible such that $\beta_m = 0$ (Delaney & McTigue, 1994; Dragoni & Piombo, 2020; Dvorak & Okamura, 1987; Got et al., 2017; Trasatti et al., 2011), and a spherical magma reservoir is embedded in an elastic half-space. An incompressible magma is a first-order simplification that allows us to focus on the role of other model variables (Delaney & McTigue, 1994; Dragoni & Piombo, 2020; Dvorak & Okamura, 1987; Got et al., 2017; Trasatti et al., 2011); the limitations of this approach and suggestions for improvements are discussed later. The wall rock compressibility for a spherical reservoir is given by $\beta_w = \frac{3}{4G}$ (McTigue, 1987), where G is the half-space shear modulus. With a further assumption that no magma leaves the chamber, mass balance states that the melt volumetric flow rate equals the time derivative of the reservoir volume:

$$Q(t) = \frac{d(\Delta V(t))}{dt}. \quad 9)$$

Substituting Equations (7) and (8) into (9) produces:

$$\frac{\mathrm{d}(\Delta P_0)}{\mathrm{dt}} = \frac{G}{\pi a^3}\frac{\mathrm{d}(\Delta V)}{\mathrm{dt}} = \frac{G}{\pi a^3}Q(t)$$

$$\frac{d(\Delta P_0)}{dt} = \frac{G\, c_r^4}{8\eta_m L_c\, a^3}(\Delta P_i - \Delta P_0 + (\rho_r - \rho_m) g L_c) \quad 10)$$

Equation (10) is a first-order linear differential equation for reservoir pressure evolution with time caused by laminar magma inflow (Le Mével et al., 2016). It can be solved analytically by

applying inlet and outlet (reservoir) pressure initial conditions. Henceforth, the term outlet pressure represents the pressure at the end of the conduit and reservoir entrance, so the outlet pressure is the same as the pressure within the reservoir (Figure 1a).

2.2 Inlet pressure boundary conditions

In this section, we examine the case of a pressure inlet boundary condition at the base of the conduit. The analytical solution is derived for a two-period piecewise inlet pressure function with different slopes (Figure 1b) to simulate the diverse temporal and phenomenological behaviour of magmatic systems.

The inlet pressure is represented as follows:

$$\Delta P_i(t) = \begin{cases} s_1\, t + P_c & , \quad 0 \le t < {t_1}^* \\ s_2\, t + {t_1}^*(s_1 - s_2) + P_c, & \quad t \ge {t_1}^* \end{cases} \quad (11)$$

where s_1 and s_2 are the slopes of pressure development with time and P_c is the initial value of the inlet pressure. By substituting equation (11) into (10) and solving the first-order linear ordinary differential equation for outlet pressure, the change in outlet pressure with time is given by:

$$\Delta P_o(t) = \begin{cases} s_1\, t + (s_1\, \tau_c - \Delta\rho g\, L_c - P_c)(e^{-\frac{t}{\tau_c}} - 1) & , \quad 0 \le t < {t_1}^* \\ s_2\, (t - \tau_c) + {t_1}^*(s_1 - s_2) + \Delta\rho g\, L_c + P_c + C\, e^{-\frac{t}{\tau_c}} & , \quad t \ge {t_1}^* \end{cases} \quad (12)$$

where τ_c is the characteristic time, the time that represents the rate of the outlet pressure development in the reservoir. τ_c is given by the following formula:

$$\tau_c = \frac{8\eta_m L_c V_0 \beta_w}{\pi c_r^4} \quad (13)$$

where $\beta_w = \frac{3}{4G}$ is the wall rock compressibility for a spherical reservoir and $V_0 = \frac{4}{3}\pi\, a^3$ is the initial volume of the spherical reservoir. C in (12) is an integration constant and can be obtained by applying the continuity condition that $\Delta P_o(t)$ is continuous at $t = t_1^*$ to give:

$$C = (s_1\tau_c - \Delta\rho g L_c - P_c) + \tau_c(s_2 - s_1)e^{\frac{t_1^*}{\tau_c}}.$$

The magma flow rate can be derived from Poiseuille's law given in equation (7):

$$\Delta Q_i(t) = \frac{\pi c_r^4}{8\eta_m L_c} \begin{cases} s_1\tau_c + (P_c + \Delta\rho g L_c - s_1\tau_c)e^{\frac{-t}{\tau_c}} & , \quad 0 \le t < {t_1}^* \\ s_2\tau_c - Ce^{\frac{-t}{\tau_c}} & , \quad t \ge {t_1}^* \end{cases} \quad 14)$$

Substituting equation (8) into the Mogi model (Mogi, 1958) for the vertical ground displacement at any point at the free surface gives:

$$u_z(t) = \frac{(1-\nu)\Delta V}{\pi} \frac{d}{(r^2+d^2)^{\frac{3}{2}}} = \frac{(1-\nu)\, d\, a^3}{3(r^2+d^2)^{\frac{3}{2}}} \Delta P_o(t) \quad 15)$$

where r, ν, and d are the radial coordinate along the free surface, Poisson's ratio, and the source depth, respectively. Applying the outlet pressure in equation (12) to equation (15) gives the vertical displacement evolution with time:

$$u_z(t) = \frac{(1-\nu)\, d\, a^3}{G(r^2+d^2)^{\frac{3}{2}}} \begin{cases} s_1\, t + (s_1\,\tau_c - \Delta\rho g\, L_c - P_c)(e^{-\frac{t}{\tau_c}} - 1) & , \quad 0 \le t < {t_1}^* \\ s_2\,(t-\tau_c) + {t_1}^*(s_1 - s_2) + \Delta\rho g L_c - P_c + C\, e^{-\frac{t}{\tau_c}} & , \quad t \ge {t_1}^* \end{cases} \quad (16)$$

These solutions are in a general form and can be reduced to three special cases: i) constant inlet pressure ($s_1 = 0$, $s_2 = 0$, $P_i = P_c$), ii) linearly increasing pressure ($s_1 = s_2$), and iii) ramped inlet pressure ($s_2 = 0$) (Figure 1b; Le Mével et al., 2016). These special cases are explored in section 4.1.1. Similar equations can be derived using the same approach for the horizontal/radial component of surface deformation. It is important to note that the development of radial displacement over time has the same rate as the vertical displacement because they are both a function of pressure, which is the only variable changing with time. For this reason, we only show the vertical displacement in the following sections.

2.3 Inlet volumetric flow rate boundary condition

An alternative method for investigating the temporal development of reservoir pressure is by defining an inlet volumetric flow rate boundary condition. To maintain a constant volume flux through the system, the pressure difference between the source and the reservoir should remain constant.

As in the previous section, we consider the volumetric flow rate to be a piecewise function of two different periods with different slopes s_1 and s_2 (Figure 1b). The inlet volumetric flow rate (Q_i) is represented as

$$\Delta Q_i(t) = \begin{cases} s_1\, t + Q_C & , \quad 0 \le t < {t_1}^* \\ s_2\, t + {t_1}^*(s_1 - s_2) + Q_C & , \quad t \ge {t_1}^* \end{cases} \qquad 17)$$

The reservoir volume change associated with a volumetric flow rate intrusion is obtained by integrating the volumetric flow rate with time; the reservoir pressure related to the volume change is given by equation (8).

$$\mathrm{Q_i} = \frac{d(\Delta V)}{dt} \;\rightarrow\; \Delta V = \int_0^t Q_i(t)dt = \Delta P_o \frac{\pi a^3}{G} \;\rightarrow\; \Delta P_o = \frac{G}{\pi a^3}\int_0^t Q_i(t)dt \qquad (18)$$

By integrating the volumetric flow rate in equation (17) over the intrusion time and substituting into equation (18), the outlet pressure associated with the magma intrusion is

$$\Delta P_o(t) = \frac{G}{\pi a^3}\begin{cases} s_1\frac{t^2}{2} + Q_C\,\mathrm{t} & , \quad 0 \le t < {t_1}^* \\ s_2\frac{t^2}{2} + t_1^*(s_1 - s_2)(t - t_1^*) + \frac{t_1^{*2}}{2}(s1 - s2) + Q_C\,\mathrm{t}, & \quad t \ge {t_1}^* \end{cases} \qquad (19)$$

Equation (19) shows that the volumetric flow rate boundary condition does not depend on the conduit dimensions, in contrast to equation (12). The inlet mass flow boundary condition eliminates the dependence on the conduit dimension and magma viscosity in the simulation of magma migration into the shallower region (reservoir) of greater melt content. The vertical displacement associated with the reservoir overpressure from magma intrusion is given by substituting equation (19) into the Mogi model shown in equation (15):

$$u_z(t) = \frac{(1-\nu)\,d}{\pi\,(r^2 + d^2)^{\frac{3}{2}}}\begin{cases} s_1\frac{t^2}{2} + Q_C\,\mathrm{t} & , \quad 0 \le t < {t_1}^* \\ s_2\frac{t^2}{2} + t_1^*(s_1 - s_2)(t - t_1^*) + \frac{t_1^{*2}}{2}(s1 - s2) + Q_C\,\mathrm{t}, & \quad t \ge {t_1}^* \end{cases} \qquad (20)$$

Similar equations can be derived using the same approach for the horizontal/radial component of surface deformation.

2.4 Magma Emplacement Processes

The understanding of magma transport through the crust is a major aspect when incorporating fluid dynamics in volcano deformation modelling. Magma transport through host rocks may occur by either brittle (e.g. sills, dykes and laccoliths) or ductile (e.g. diapirism) mechanisms (Sparks et al., 2019), although there are diverse views on exactly how magma ascends through the crust and accumulates in crustal reservoirs, as well as on the architecture of crustal-scale magma plumbing systems (Annen et al., 2015). The diversity of understanding reflects the range of approaches implemented to study magma plumbing systems (e.g. physical, geochemical and petrological) and differences between the characteristics of the exposed geological record and direct geophysical observations (Cruden & Weinberg, 2018; Lengliné et al., 2008; Reverso et al., 2014). Thus, a fundamental challenge for dynamic volcano deformation modelling is determining the most realistic (or suitable) conceptual model and boundary conditions for magma transport. We implement the conduit-reservoir conceptual model for simplicity and then discuss the applications and implications of our approach. For boundary conditions, we use either a defined pressure or mass flow with a piecewise function consisting of constant or increasing/decreasing segments (Figure 1b). Regardless of the exact magma transport mechanism (e.g., via dykes, conduit, flush percolation), a constant defined pressure or flow boundary condition is used to represent a steady magma supply, while a boundary condition of increasing or decreasing pressure or flow with time represents time-variable magma supply.

3. Numerical modelling

3.1 Setup and Geometry

The Finite Element (FE) numerical models were built and solved using the fluid-structure interaction (FSI) module in COMSOL Multiphysics® v5.2. Our numerical modelling comprises four fundamental steps: 1) corresponds to constructing the model geometry; 2) specifies the multiphysics models, including fluid dynamics, solid mechanics, and fluid-structure coupling with definition of initial and boundary conditions; 3) creates and optimizes the mesh; and 4) selects a suitable numerical solver. In step 1 we construct a 2D axisymmetric geometry with an r-dimension of 30 km and z-dimension of 50 km; this is large enough so that the deformation and stresses induced by the magma reservoir are unaffected by the external boundary conditions of the models. The model comprises a vertical conduit of length L_c and radius c_r connected with a

spherical shallow reservoir (Figure 2a). Since the flow, and thus the stress distribution, is axisymmetric, we solve the problem in a single plane and apply symmetric boundary conditions on the symmetry axis. The source, melt, and half-space characteristics were determined for a range of parameters (Table 1).

Step 2 combines fluid flow dynamics with solid mechanics to capture the two-way interaction between the fluid and the solid structure. The fluid flow is described by the Navier-Stokes equations, which solve for the fluid velocity field and the pressure. The total force exerted on the solid boundary by the fluid is equal to the sum of the pressure and viscous forces in the fluid, which loads the solid boundaries. Two schemes of inlet boundary condition – the inlet pressure and the inlet mass flow rate – are applied to the base of the conduit. For each scheme, two cases of inlet pressure or mass flow rate are considered. We first consider constant inlet pressure and constant inlet mass flow rate. We then consider a piecewise function for both the inlet pressure and inlet mass flow (Figure 1b). In step 3, the mesh includes 29,000 triangles and 3620 quads. The mesh is refined at crucial boundaries, especially around the reservoir and at the free surface (Figure 2b). The model domain is also divided into two areas, the first being the area comprising the reservoir, the conduit and the wall rock close to it, which is finely meshed, while the second area farther from the reservoir is more coarsely meshed (Figure 2b). A time-dependent (PARDISO) solver is chosen in step 4 to solve the Navier-Stokes equations for the fluid and the continuum mechanics equations for the solid.

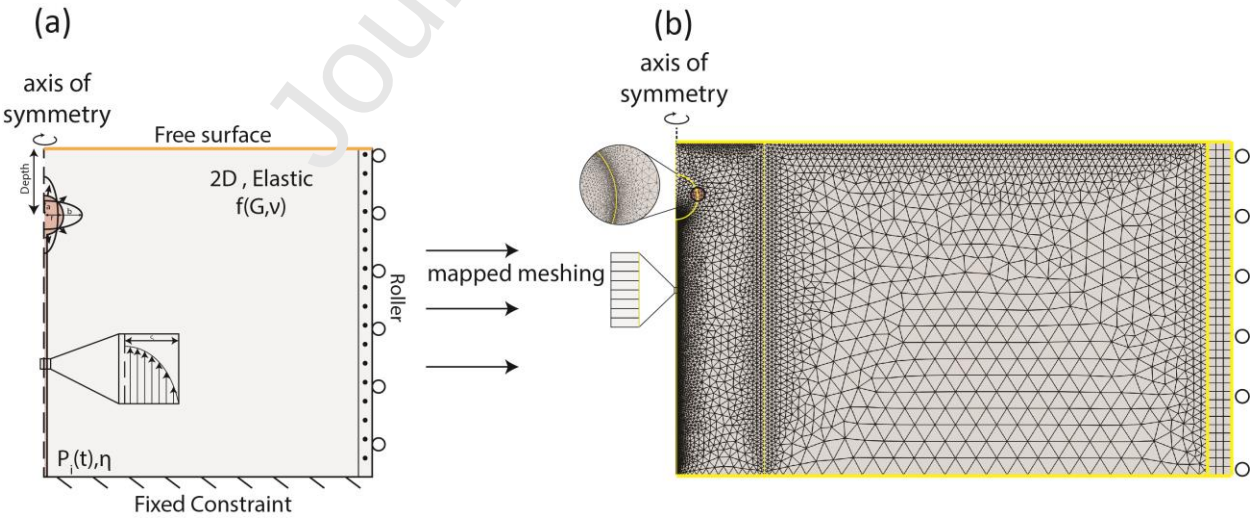

Figure 2. *Setup of the numerical models. (a) Schematic illustration of the model of laminar flow into a magma-filled spherical or ellipsoidal reservoir connected to a vertical conduit. The top of the model space is a free surface, the*

base of the model is fixed, the left-hand boundary is an axis of symmetry and the right-hand boundary has a roller condition. The dotted region on the right side of the model geometry is an infinite element domain. Fluid-flow boundary conditions are applied to the base of the conduit. (b) The meshed domain of the numerical model. The mesh is selected to be refined at the crucial boundaries, especially around the reservoir and at the free surface. The mesh includes 29,000 triangles and 3620 quads.

Table 1. *List of Model Parameters.*

Parameter	Symbol	Unit	Value	Reference
Source parameters				
Conduit radius	c_r	m	30, 20	(Aravena et al., 2018; Massol et al., 2001)
Conduit length	L_c	km	20.5, 21	(Hammond et al., 2011)
Spherical reservoir radius	a_{sp}	km	1.5, 2	(Hautmann et al., 2010; Hickey & Gottsmann, 2014)
The reservoir central depth	d	km	7.5	-
Melt properties				
Viscosity of magma	η_m	Pa s	5×10^8, 5×10^9	(Kilburn, 2000)
Density of magma	ρ_m	kg m^{-3}	2600	(Gudmundsson, 2020)
Half-space characteristics				
Shear modulus	G	GPa	20	(Gudmundsson, 2020)
Density of crustal rocks	ρ_r	kg m^{-3}	2600	(Carmichael, 2017)
Poisson's ratio	ν	-	0.25	(Gudmundsson, 2020)
Conduit boundary conditions				
Maximum inlet pressure	$\Delta P_{i_{max}}$	MPa	10	(Head et al., 2021; Le Mével et al., 2016)
Maximum inlet volumetric flow rate	$Q_{i_{max}}$	$m^3\ s^{-1}$	0.1	(Nooner & Chadwick, 2009)

3.2 Modelling approach

To benchmark our numerical models to the analytical solutions for the different inlet boundary condition approaches, and then to conduct further sensitivity analyses of the numerical setup, we ran a series of forward models. For the benchmarking, the modelled spherical reservoir source has a radius of 1.5 km, a central depth of 7.5 km and is emplaced in an elastic medium with a shear modulus of 20 GPa. More sensitivity tests on the shear modulus have also been added to the supporting information (Figure S1). We assume that the feeding conduit extends from the base of the crust to the shallow reservoir, so we use a value for conduit length based on

the average continental crust thickness in volcanic areas (Hammond et al., 2011; MacKenzie et al., 2008; Suhardja et al., 2020). The predicted surface displacements in the FEM models for various inlet conditions are compared with the results obtained from the analytical solutions. For the FEM sensitivity tests, we also considered oblate and prolate reservoir geometries. For an inlet pressure boundary condition, the pressure development was calculated for a set of magma characteristics (viscosities) and conduit dimensions (radii) as shown in Table 1. Two values of magma viscosity ($\eta_m = 5 \times 10^8$ & 5×10^9 Pa s) are used to highlight the effect of one order of magnitude difference in magma viscosity on reservoir pressure evolution. We conducted our analyses across a wider range of viscosities, capturing both basaltic and silicic systems, but display only two values for simplicity of graphical representation. We use high viscosity values because the faster response of lower viscosity magmas masks the detail seen in the high viscosity results. Due to the lack of direct observation to constrain the size of a vertical feeding conduit, we consider a wide range of conduit radii varying from 5 m to 50 m (Aravena et al., 2018; Massol et al., 2001). For the inlet mass flow scheme, the development of reservoir pressure does not depend on the magma and the conduit characteristics; here we applied different inlet volumetric flow rate functions with time.

In this study, we do not consider wall rock failure, so we use values for the boundary conditions that generate reservoir pressures below the critical 'failure' overpressure for the given reservoir depth and geometry (Currenti & Williams, 2014; Gerbault et al., 2018). A full exploration of failure criteria is beyond the scope of our current study. To simplify the numerical simulation, and focus our efforts on the effects of magma viscosity and pressure or magma flow boundary conditions, we do not account for a separate buoyancy force arising from a density contrast between the rock and magma. We consider that the inlet pressure/mass flow comprises both the pressure caused by the buoyancy force and the pressurization associated with magma injection. The FEM models take approximately 10 minutes to solve when using a mesh that has been successfully benchmarked against the analytical solution.

4. Results

4.1 Benchmarking

This section validates the numerical solution against the analytical solution provided in section 2 for a range of model parameters.

4.1.1 Inlet pressure

Here we benchmarked the fluid-structure interaction FEM model against the derived analytical solution for the inlet pressure boundary condition. The analyses were conducted on three cases of inlet pressure. Case I uses a constant inlet pressure applied at the conduit base. Case II represents a linearly increasing inlet pressure. Case III uses a ramped inlet pressure function (Figure 3a and Supplementary Table S1). Two magma viscosities ($\eta_m = 5 \times 10^8$ & 5×10^9 $Pa\ s$) were used in this analysis to highlight their influence on the pressure development and flow rate.

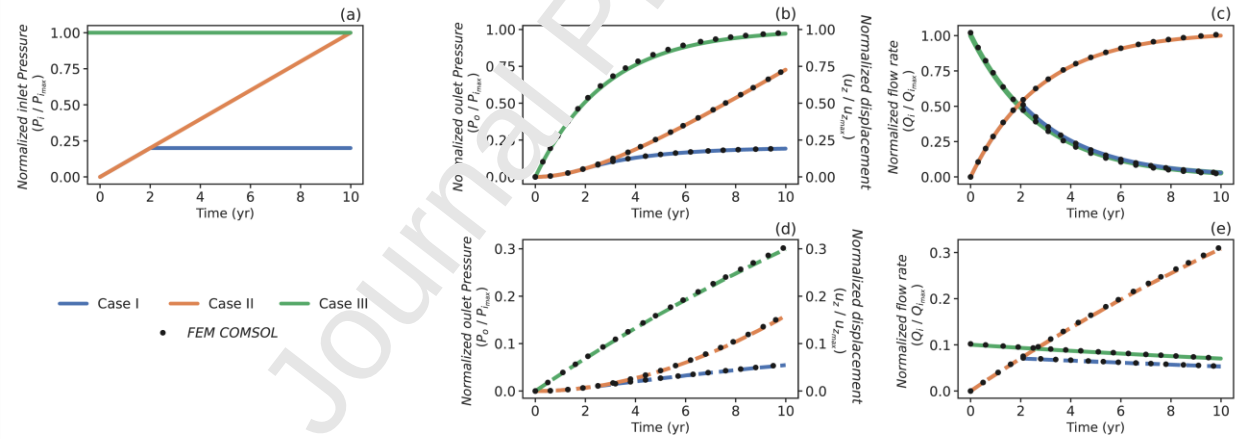

Figure 3. *Inlet pressure boundary condition results. The model has a spherical reservoir of radius 1.5 km located at a depth d = 7.5 km, which is connected to a conduit of radius 20 m. (a) The inlet pressure functions defined at the conduit base. (b) and (d) show the normalized pressure development in the reservoir and the normalized vertical surface displacement for a* 5×10^8 *Pa s magma viscosity (b, solid line) and a* 5×10^9 *Pa s magma viscosity (d, dashed line). The values are normalized to the maximum value of inlet pressure* (1×10^7 *Pa) and surface displacement (2.4 cm). (c) and (e) show the normalized inlet flow rate supplied to the reservoir for the two magma viscosities* (5×10^8 *Pa s solid line (c), and* 5×10^9 *Pa s dashed line (e)). The values of the inlet volumetric flow rate are normalized to the maximum value for the lower viscosity magma analysis (0.056* $m^3\ s^{-1}$*). The lines of*

various colours represent the analytical models and the dotted lines in (b) – (e) show the results acquired from the numerical model using COMSOL.

In general, the pressure develops more rapidly in the reservoir for the lower viscosity magma (Figure 3b) than for the more viscous magma (Figure 3d), producing a greater amount of surface deformation within a given timeframe. For a constant inlet pressure, the rapid development of reservoir pressure for the lower viscosity magma means the pressure differential between the reservoir and base of the conduit rapidly diminishes, which is reflected in the quick decrease of the flow rate (Figure 3c), and the deceleration of the inflation rate (Figure 3b). The characteristic time is longer for magmas with higher viscosity because of the larger resisting viscous drag force. Hence, the pressure difference is sustained over an extended period and the flow rate and temporal surface deformation decreases more slowly (Figure 3e). Time series that have not been normalized and extended results can be found in the supporting information in Figures S2 & S3.

4.1.2 Inlet flow rate

In this section, we benchmark the FEM model solutions against the derived mass inlet flow analytical solution (Figure 4). Instead of applying an inlet pressure, we define a volumetric flow rate boundary condition at the conduit base and explore the pressure development in the shallow reservoir as the magma is injected. Here the conduit does not affect development of reservoir pressure, so the same pressure is generated whether we apply the mass flow boundary condition at the conduit base or reservoir base.

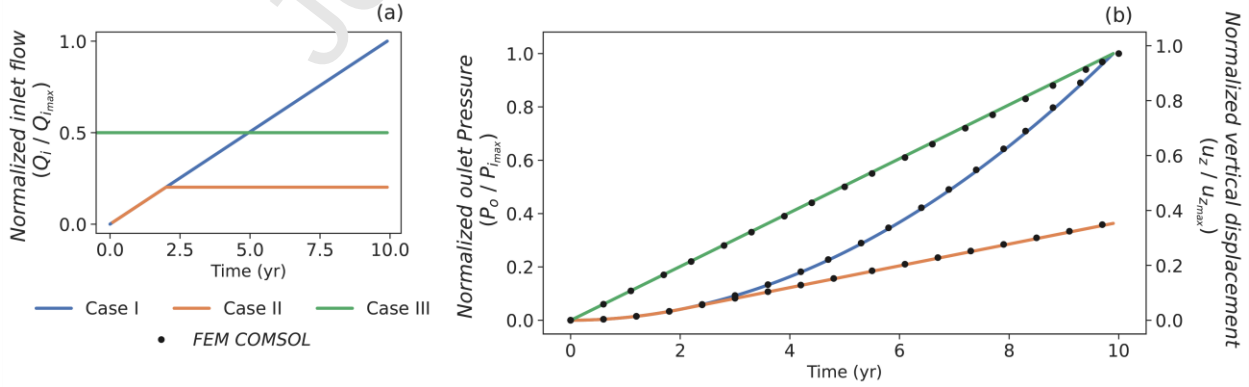

Figure 4*. Inlet flow rate boundary condition results. The model has a spherical reservoir of radius 1.5 km located at a depth d = 7.5 km, which is connected to a conduit of radius 20 m. (a) Three inlet volumetric flow rate functions for magmas injected into the conduit base; inlet mass flow rate values are normalized to the maximum value of the inlet*

flow rate (0.1 $m^3\ s^{-1}$). (b) The pressure development is a quadratic form with time as the mass inlet flow increases (Case I, blue line) and linearly increasing for the constant inlet mass flow function (Case III, green line); pressure values are normalized to the maximum value of outlet pressure ($3 \times 10^7 Pa$), and the vertical displacement results are normalized to the maximum value of vertical deformation ($u_{z_{max}} = 7.5$ cm). The dotted lines are the results from the numerical model obtained using COMSOL.

For a constant volumetric flow rate (Figure 4, green line), the reservoir pressure and surface deformation increase linearly with time, with a rate dependent only on the value of mass flow rate and the initial reservoir radius (c.f. equation (12)). As the system is closed and the injected (incompressible) magma is constrained by the plumbing system, the reservoir pressure development (and surface deformation) is independent of the magma and conduit properties. For a linearly increasing volumetric flow rate, the outlet pressure and surface deformation is parabolic (rate-increasing) with time (Figure 4, blue line) and proportional to the basal magma inflow, the crustal rigidity, and the geometry of the magma reservoir. The temporal vertical deformation rate is the same as the pressure evolution with time, but the absolute values of deformation are also controlled by the inlet flow rate magnitude, and reservoir shape and depth. Further results for different constant inlet flow rates are shown in Supplementary Figure S6.

4.2 Numerical sensitivity analyses

This section reviews the dynamics of magma reservoir pressurization and associated surface displacement for the two schemes of magma intrusion whilst considering more complex reservoir geometries. Three different reservoir geometries are considered – spherical, oblate and prolate – to highlight the effect of different geometries, as well as magma supply characteristics, on system dynamics. All the selected geometries have the same volume, which is equivalent to a spherical reservoir of radius 2 km. The prolate and oblate geometries have aspect ratios of a/b = 5 & 0.2, respectively, where a and b are the major and minor axes (Figure 2a). Radial displacement changes with time at the same rate as the vertical displacement, so this section shows only vertical displacement. The results for radial displacement over time are shown in the supplementary material (Figures S4, S7 and S8).

4.2.1 Inlet pressure boundary condition

We focus on the case of a constant inlet pressure boundary condition and use the same two magma viscosities as the benchmark tests ($\eta_m = 5 \times 10^8$ & 5×10^9 $Pa\ s$), and conduit radii of 20 and 30 m.

4.2.1.1 Pressure and deformation evolution

Understanding the pressure development in the magma reservoir, and the parameters controlling it, are fundamental for understanding the surface deformation generated. Figure 5 shows the reservoir pressure and deformation evolution with time for a constant inlet pressure at the conduit base. Pressure increases are faster for spherical and prolate reservoirs compared to the oblate reservoir because of different reservoir compressibilities. The spherical and prolate reservoirs have roughly the same pressure development rate because the two geometries have similar compressibilities: $\beta_w^{Pr} = \frac{4}{3}\beta_w^{Sp} = \frac{1}{G}$ (Amoruso & Crescentini, 2009), where β_w^{Pr} and β_w^{Sp} are the prolate and spherical reservoir compressibilities, respectively. The oblate geometry is highly compressible, given by $\beta_w^{Ob} = \frac{1}{G}\left(\frac{2}{2\pi}\frac{a}{c} - \frac{3}{5}\right)$, and thus has the longest characteristic time (c.f. equation (17)). Reservoir pressure increases more slowly (longer characteristic time) for higher viscosity magmas and narrower conduits due to the downward viscous force opposing the flow. Figure 6 extends this analysis to show the characteristic times for a range of magma viscosities and conduit radii. In a spherical reservoir with a low viscosity magma intrusion (1×10^5 $Pa\ s$), the characteristic times range from 0.3 hours for a 50 m conduit to 124 days for a 5 m conduit, while the characteristic time for a high viscosity magma (1×10^{10} Pa s) increases from 4 years for a 50 m conduit to thousands of years for a 5 m conduit.

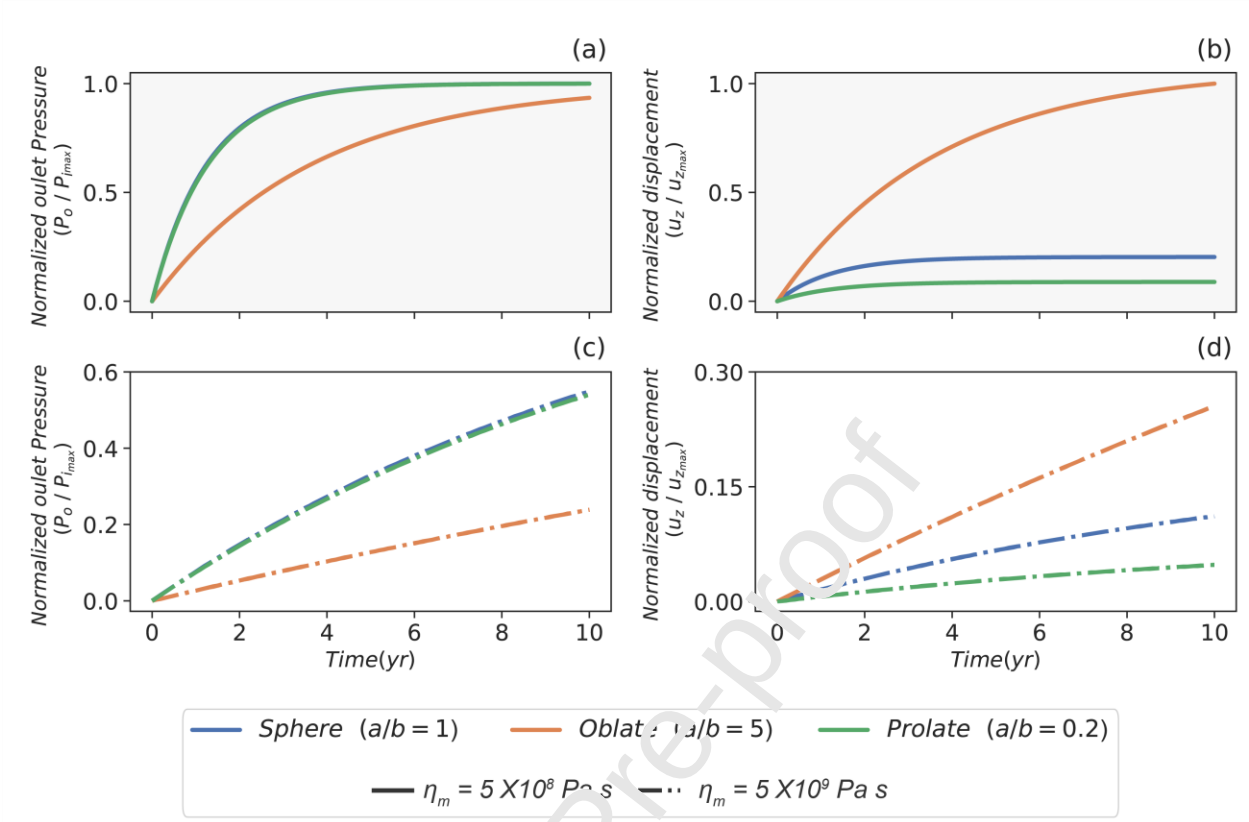

***Figure* 5.** *Reservoir pressure development with time for three magma reservoir geometries at a depth of 7.5 km, computed numerically for a constant inlet conduit pressure boundary condition at the base of a 30 m conduit radius. (a) and (c) Normalized pressure trend over time for a* 5×10^8 *(a, solid line) and a* 5×10^9 *(c, dashed-dotted line) Pa s viscosity magma. (b) and (d) Normalized vertical deformation trend over time evaluated directly above the center of the source, at z = r = 0 for a* 5×10^8 *(b, solid line) and a* 5×10^9 *(d, dashed-dotted line) Pa s viscosity magma. The results of the pressure are normalized to the value of the inlet pressure (*1×10^7 *Pa), and the results of the vertical deformation are normalized to the maximum vertical displacement value (*$u_{z_{max}} = 28$ *cm).*

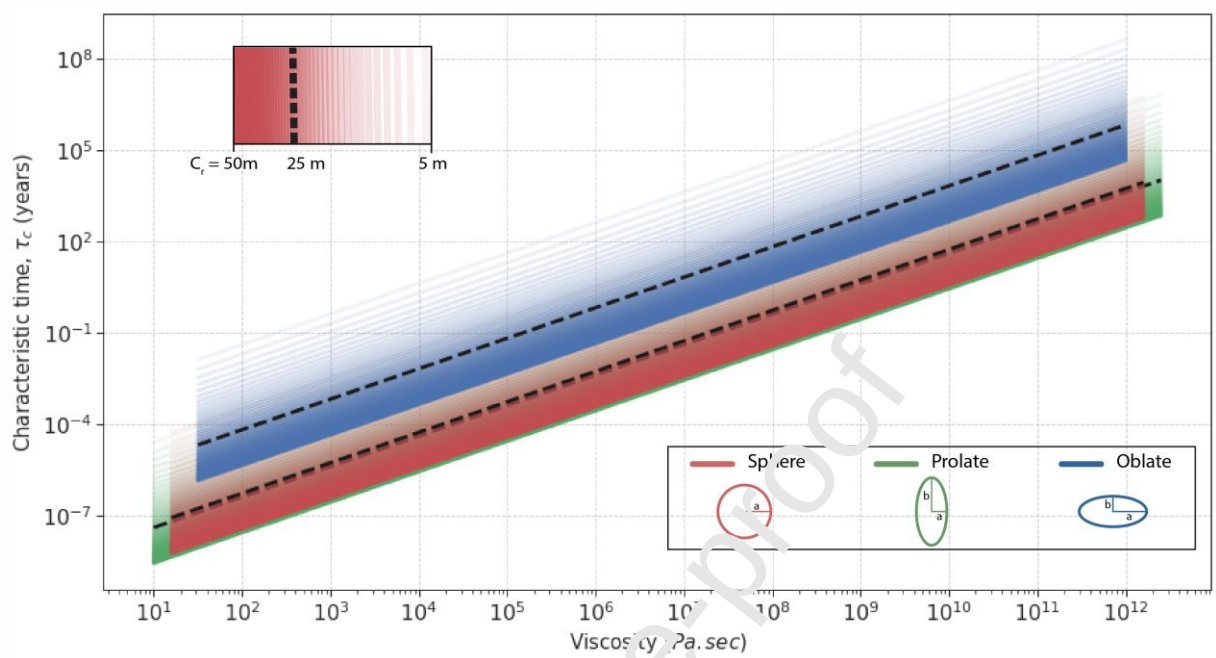

Figure 6. *The characteristic time τ_c for a wide range of magma viscosities (basalt – rhyolite, 1e1 – 5e12 Pa s) and conduit radii (5 -50 m). The line transparency changes with conduit radius. The dashed line represents the values for the mid-value of conduit radius cr=25 m. The spherical and prolate geometries have very similar characteristic times due to their comparable compressibilities.*

The modelled surface deformation evolves in parallel with reservoir pressure. The temporal deformation rate depends on the conduit radius and magma viscosity via the time-dependence of reservoir pressurization. Figure 5 shows the time scales of surface deformation for the three magma reservoir geometries and two magma viscosities. The amplitude of the vertical and radial deformation rates is proportional to the reservoir geometry and its overpressure; an oblate geometry deforms more than the spherical and prolate geometries despite the lowest rate of pressure increase. The overpressure is sensitive to the magma viscosity, the conduit dimensions, and the inlet pressure value, while the vertical (and horizontal) displacement is also sensitive to reservoir shape: oblate geometries are more efficient at generating vertical displacement than prolate geometries, which are capable of producing relatively more horizontal deformation (Dzurisin, 2006; Segall, 2019). Decreasing-rate uplift patterns, similar to those in Figure 5, have been observed at Yellowstone caldera, USA (Chang et al., 2010) and Tungurahua volcano, Ecuador (Morales Rivera et al., 2016).

4.2.1.2 Flow rate evolution

For an inlet pressure boundary condition, the flow rate is highest when the pressure difference between the reservoir and conduit base is greatest and falls to zero as the pressure difference diminishes with time (Figure 7). For a lower viscosity magma or wider conduit, the reservoir pressure increase is rapid as the viscous drag force is small (e.g. Figure 5a). Accordingly, the flow rate is maximum at the start of the intrusion and rapidly drops to zero (e.g., Figure 7a). The deceleration of flow rate is more muted for a higher viscosity magma or narrower conduit.

The longer characteristic time for the oblate reservoir geometry means that the pressure difference between the source and the reservoir decreases slowly relative to the other geometries, so the mass delivery is sustained for longer. In contrast, for both the spherical and prolate reservoir, where the characteristic time is shorter than for the oblate geometry, the flow rate decreases more rapidly.

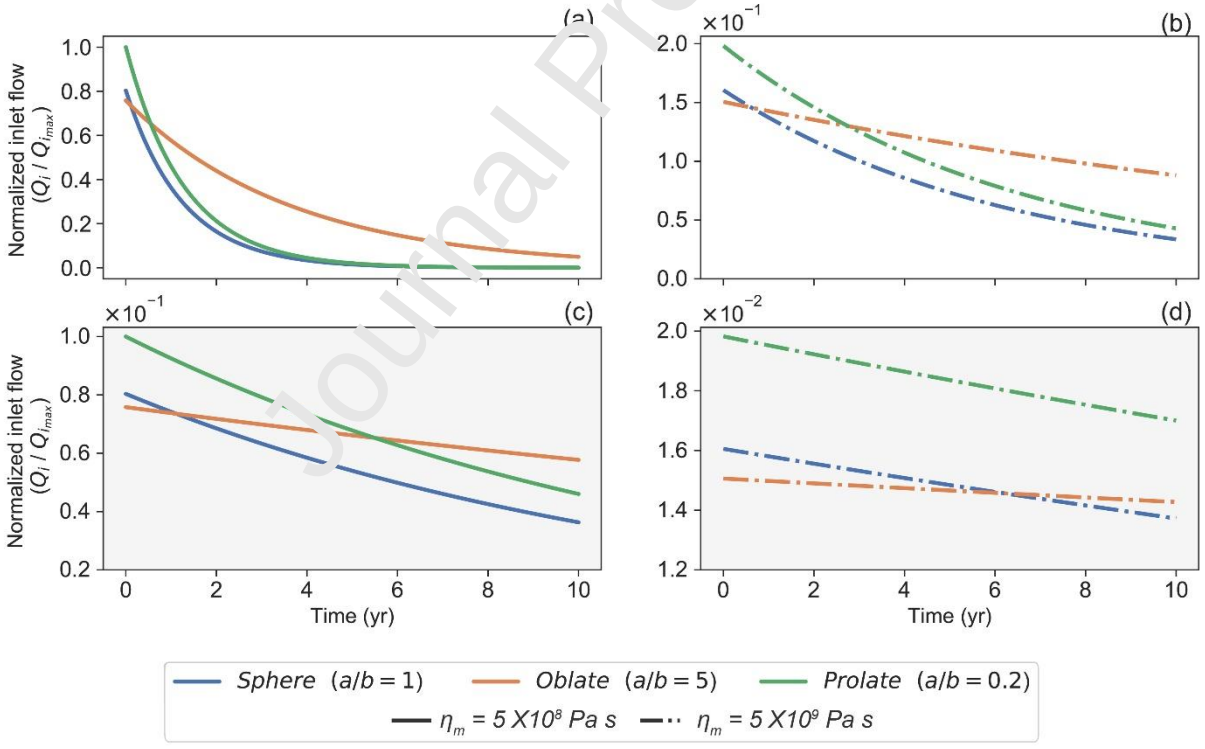

Figure 7. *Flow rate development with time for three magma reservoir geometries at a depth of 7.5 km computed numerically for a constant inlet pressure boundary condition. (a) and (b) The flow rate delivered to the reservoir for two different viscosity magmas ($\eta_m = 5 \times 10^8\ (a, solid\ line)\ \&\ 5 \times 10^9\ (b, dashed - dotted\ line)\ Pa\ s$) for a 30 m conduit. (c) and (d) The same as for (a) and (b) but for a 20 m radius conduit. The results are normalized to the*

maximum value of inflow rate for the case of a 5×10^8 *Pa s magma intrusion into 30 m radius conduit (*$Q_{imax} = 0.38\ m^3\ s^{-1}$*).*

4.2.2 Constrained inlet flow rate boundary condition

This section considers an inlet mass flow boundary condition for a range of reservoir geometries. This scheme prescribes a defined mass flow, thereby focusing on the net effect of mass addition to the reservoir regardless of the parameters that influence the pressure difference or the mechanism of magma transport from depth. We show the temporal evolution of reservoir pressure and the resultant surface deformation for different mass flow rates (Figure 8). Magma viscosity and conduit width are held constant as the results are independent of magma properties and the feeding system geometry.

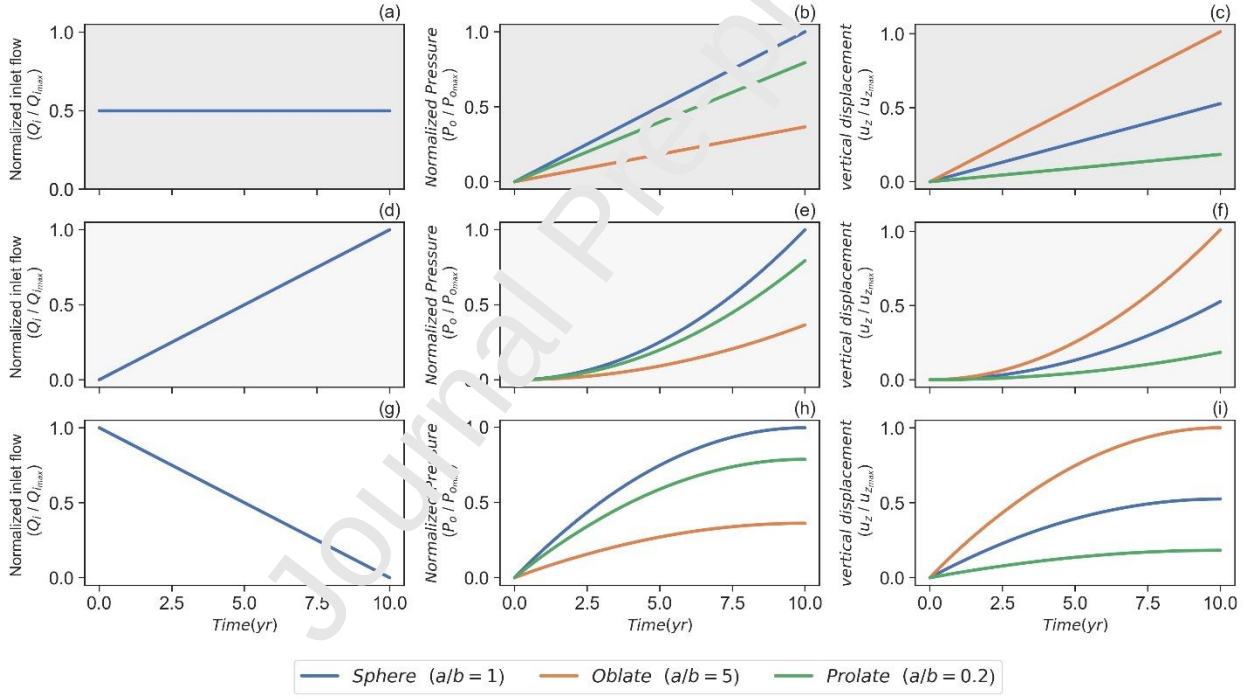

Figure 8. *Reservoir pressure and surface deformation with time from three inlet mass flow functions for three reservoir geometries. (b) and (c) The reservoir pressure (b) and resultant vertical surface deformation (c) with time when the mass inlet flow is constant (a). (e) and (f) Same as for (b) and (c) but for an inlet mass flow rate that linearly increases with time (d). (h) and (i) Same as for (b) and (c) but for a mass inlet flow that is linearly decreasing with time (g). The flow rate column (a, d, g) is normalized to the maximum value of inflow (*$Q_{imax} = 0.1\ m^3\ s^{-1}$*). The pressure column (b, e, h) is normalized to the maximum value of outlet pressure (*$P_{o_{max}} = 1.2 \times 10^7\ Pa$*). The vertical displacement column (c, f, i) is normalized to the maximum value of vertical displacement (*$u_{z_{max}} = 13\ cm$*).*

A constant flow rate produces a linear development of pressure with time, with a slope proportional to the inlet mass flow and the reservoir geometry (Figure 8a-c). The rate of pressure increase is greatest for the spherical reservoir (low compressibility), and lowest for the highly compressible oblate reservoir. Predictably, the oblate reservoir shows the greatest amplitude of vertical deformation due to the large surface area and vertical reservoir deformation. For all three reservoir geometries, however, the surface deformation rate is linear and mirrors the temporal evolution of reservoir pressure; radial displacements show the same temporal development (Figure S7). The outlet pressure for a linearly increasing (Figure 8e) or linearly decreasing (Figure 8h) inlet mass flow function is quadratic in form, showing accelerating or decelerating pressure increase with time, respectively. The resultant surface deformation shows the same temporal patterns as the reservoir pressure (Figure 8 f & i). In general, the reservoir pressure is the temporal integration of the inlet mass flow, such that a constant inlet flow rate leads to linear outlet pressure, and a linearly increasing/decreasing inlet mass flow leads to a quadratic outlet pressure. The analyses shown in Figure 8 were designed to maintain a constant magma mass injected for all the three inlet functions; for this reason, the final values of outlet pressure and surface deformation are the same. A linear trend of surface deformation, similar to Figure 8c, has been observed at Laguna del Maule volcanic field, Chile (Mével et al., 2015), and Reventador and Cerro Auquihuato volcanoes (Morales Rivera et al., 2016), while a rate-decreasing deformation trend, similar to Figure 8i, has been recorded at the Three Sisters volcanic centre, USA (Dzurisin et al., 2009).

5. Discussion

The dynamics of magma intrusion, migration and accumulation control the resultant spatial and temporal evolution of surface displacement. With advances in temporal deformation monitoring through continuous GPS observations and InSAR time-series, we can now analyze the time-dependent deformation behaviour of volcanoes to improve hazard assessments. Advances in monitoring can be mirrored with improvements in volcano deformation modelling; our study, which replaces kinematic studies with dynamic numerical models that couple solid mechanics and fluid dynamics, shows a possible path forward.

Many numerical studies of volcano deformation focus on the response of the surrounding host rock to magma reservoir overpressure but ignore the melt injection dynamics driving the

pressure and volume changes (Head et al., 2019; Hickey et al., 2013; Johnson et al., 2019; Masterlark, 2007; Pascal et al., 2014). These studies are useful for understanding the host rock behaviour, but do not have the correct underpinning physics to interpret the temporal evolution of magma pressure and surface deformation. Our first-order analytical and numerical results provide insights into the coupled fluid and solid behaviour of a magmatic plumbing system, as well as the resulting reservoir pressurization and surface deformation. With different reservoir geometries, for the first time we show pressurization is controlled by geometric compressibility. Pressurization is faster for spherical- and prolate-shaped reservoirs because of their lower compressibility, whereas pressurization is slower for oblate-shaped reservoirs due to their higher compressibility.

Reservoir pressurization also depends on magma compressibility because of compaction (volume reduction) of compressible magma in the reservoir, which creates additional space to accommodate injected melt without enlargement of the reservoir, and can modify the time-dependent response. For this reason, the change in reservoir volume that causes inflation with a compressible magma requires a greater mass compared to the case of incompressible magma injection (Huppert & Woods, 2002; Kilbride et al., 2016). Here we assume an incompressible magma to simplify the computations and focus on the effects of the geometry and magma viscosity of the plumbing system. The limitations and lessons learned from this approach are discussed later.

We considered two boundary conditions: a defined inlet pressure or mass flow rate. Patterns of pressurization and surface deformation in the former are sensitive to the geometry of the deep feeder system (here, conduit radius) and magma viscosity (Figure 6). For a constant inlet pressure, the reservoir pressure increases at an exponentially decreasing rate defined by the characteristic time (Figure 3). For a more viscous magma or narrow conduit radius, a "near-linear" long term reservoir pressurization is established, reflecting the longer characteristic time (equation 13) from the greater viscous drag force (Figure 3d). In contrast, a lower viscosity magma allows a faster response to the inlet conduit pressure, producing rapid changes in reservoir pressure, flow rate and surface deformation. For our model setup, and the inlet pressure driving force, lower viscosity magmas produce faster surface deformation rates; the first time magma viscosity has been linked to volcano deformation patterns.

The sensitivity of the inlet pressure boundary condition models to the nature of the feeder system presents a challenge for interpreting deformation data because it is difficult to constrain conduit dimensions. Moreover, magmatic systems may be transcrustal and complex in form such that magma may migrate from the mid crust to the upper crust through multiple dykes and sills, and/or through mush layers, rather than single cylindrical conduits (Cashman et al., 2017; Edmonds et al., 2019; Lipman & Bachmann, 2015). The inlet mass flow boundary condition model setup, in contrast, is independent of the conduit dimensions and dictates that some amount of magma will be delivered regardless of the feeder system geometry. Under these conditions, time-dependent pressurization and surface deformation depend primarily on the mass flow rate of magma supplied to the reservoir.

The independence of the inlet mass flow boundary condition model setup to conduit dimensions means that identical results are obtained if the modelled conduit is removed entirely from the model geometry, and the inlet boundary condition with mass inflow is directly applied to the base of the reservoir. From this perspective, the inlet mass flow modelling scheme could potentially provide a better fit to the evolving view of a TCMS (Hildreth, 2004; Jackson et al., 2003, 2018; Lipman & Bachmann, 2015; Sinton & Detrick, 1992; Sparks et al., 2019). It bypasses and simplifies the exact make-up of the system beneath the shallow reservoir (i.e. it moves away from a conduit-chamber concept, a dyke/sill complex, or percolation of magma through mush layers) and instead focuses directly on the transfer of a volume of magma (Q_i) from within or beneath a TCMS to the shallow melt-dominated reservoir at the top of a TCMS responsible for generating surface deformation (Figure 9). This shallow melt-rich layer may expand with time due to crustal assimilation and magma replenishment from greater depths unless it erupts or is transferred to a different part of the crust (Anderson, 1976; DePaolo, 1981). The inlet mass flow model approach can be viewed as the simplified injection of a defined volume of magma into a preexisting shallow reservoir at the top of an extended TCMS (Figure 9) and could be used to interpret deformation data from volcanic unrest episodes by fitting the temporal deformation data with a mass flow intrusion function(s). We show a range of temporal magma supply functions that could be generated by different magma supply mechanisms and the time-dependent deformation they produce (Figure 8) and confirm via sensitivity analyses that in coupled solid-fluid models, the volume and temporal supply rate of magma control the temporal development of ground displacements.

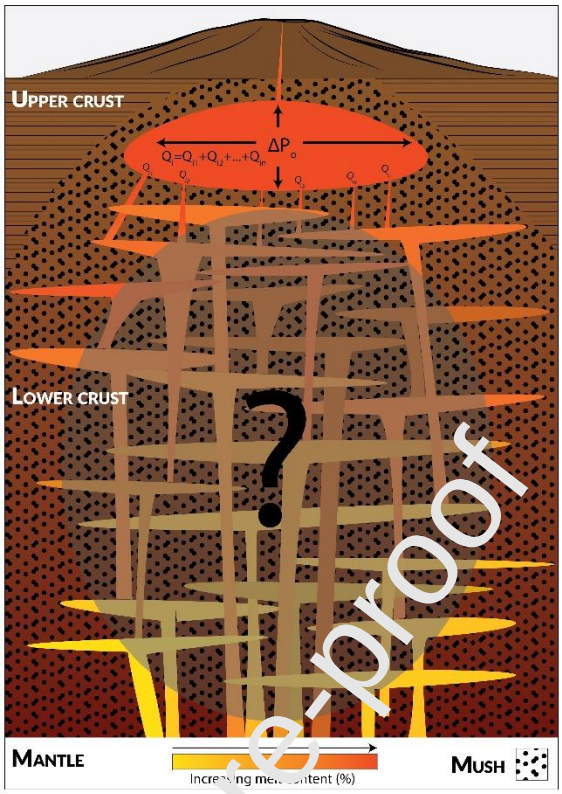

Figure 9. *Schematic diagram of a transcrustal magmatic system (TCMS) which extends from the mantle to the upper crust. The system includes a shallow melt dominated reservoir. The total amount of the inlet mass flow rate delivered to the shallow melt-dominated reservoir is equal to the summation of the mass flow rate from each of the sub-channels connected to the reservoir ($Q_i = Q_1+Q_2+...+Q_n$). Adapted from Cashman et al. (2017).*

Transport of magma still relies on a pressure gradient to drive flow but as pressure gradients, and deep magma transport geometries are currently impossible to constrain, the presented mass flow model could help simplify and expedite interpretation of deformation data for hazard assessment from assumed trans-crustal magmatic systems, where estimates of magma injection volumes are critical. For a more precise picture of the migration of magma through a vertically extensive TCMS in a crustal section, our work could be combined with future studies that focus on deep magma inflow models.

Our models, however, have limiting assumptions that must be considered, and that can be built upon for more robust application to magma system dynamics in the future. We have used a model based on simple rheologies, including linear elastic host rock behaviour and an incompressible magma intruded into a shallow, 100% melt, magma reservoir. By neglecting magma compressibility our spatial deformation amplitudes and temporal deformation rates are

likely over-estimated and should be viewed as end-member upper estimates. However, using an incompressible magma has demonstrated the role of geometric reservoir compressibility, which may have been hidden were a compressible magma used instead. A (long-standing) 100% melt magma reservoir is unlikely; more probable is a porous region of crystal mush with varying proportions of interspersed melt. In this scenario, the reservoir could be approximated as a poroelastic domain (e.g., Liao et al., 2018), where the diffusion of melt through the reservoir from an intrusion event would add additional time-dependent behavior to the solid-fluid coupling and generation of surface deformation. Partial melting experiments of igneous rock suggest that when magma cools and its crystallinity reaches a transition point (~50%) the crystals contact to form a continuous framework with interstitial melt, known as a crystal mush (Caricchi et al., 2008; Marsh, 1981; Rosenberg & Handy, 2005). Beyond this point of crystallinity, the reservoir is more appropriately modelled as a poroelastic domain (e.g., Liao et al., 2018), while at points of crystallinity lower than the transition point, the magma can still flow in a laminar regime, which we consider in our study. However, the interplay of the poroelastic response and magma compressibility should be addressed in future work. Our approach could be further developed by accounting for viscoelastic crustal behaviour and the role of volatiles on time- and depth-dependent magma properties (both viscosity and compressibility). Viscoelastic crustal behaviour would affect the temporal evolution of deformation due to creep or recovery (time-dependent) behaviors (Head et al., 2019). Volatiles will affect magma viscosity and, once exsolved, compressibility. In summary, the results presented here provide useful first-order knowledge for building more complex coupled solid mechanics- and fluid dynamics-based numerical volcano deformation models.

6. Conclusions

We present numerical and analytical solutions for magma intrusion dynamics in a shallow reservoir to explain the time evolution of volcanic surface deformation. Most volcano deformation models ignore magma intrusion dynamics and focus on the crustal response to reservoir overpressure, with the magma reservoir modelled as a cavity embedded in a half-space with a boundary load. Our models couple solid and fluid mechanics to examine reservoir pressurization and surface deformation for different geometries of a shallow (fluid-filled) magma reservoir. Analytical solutions were adapted and derived for two schemes of inlet boundary

condition; inlet pressure and inlet mass flow, using a new piecewise function to account for changing magma supply conditions with time. For the pressure inlet boundary condition, reservoir pressurization is sensitive to feeder system dimensions and magma properties. With the intrusion of a higher viscosity magma, or with a relatively narrow conduit radius, the system undergoes "near-linear" long term reservoir pressurization and surface deformation because the characteristic time is controlled by the viscous drag force. Lower viscosity magmas produce faster surface deformation rates for this model setup, highlighting a potential role of magma viscosity in determining surface deformation patterns. Associated challenges include determining realistic feeder conduit dimensions and magma properties.

We also examined a defined inlet volumetric flow rate boundary condition, which dictates that a certain magma supply rate will be delivered regardless of the feeding system geometry and magma characteristics. This scheme removes the effects of conduit geometry and magma viscosity so that time scales of reservoir pressurization and surface deformation are dependent primarily on the rate of mass flow. Results indicate that pressurization of melt-rich reservoirs are controlled by reservoir shape (the geometric compressibility); pressurization is faster for spherical- and prolate- reservoirs because of their lower compressibility, and slower for oblate reservoirs due to their higher compressibility. We tentatively suggest that the inlet mass flow boundary condition may provide a better future modelling approach for a conceptual fit to the evolving view of trans-crustal magmatic systems (compared to the inlet pressure boundary condition). The mass flow approach is not constrained by the extended feeding system and magma supply mechanics beneath the shallow reservoir occupying the top of a TCMS, which are often unknown; it instead focuses on the input mass flow rate as a function of time. This simplifying step will allow applications of the model to focus primarily on crucial temporal magma supply rates regardless of poorly constrained magma supply mechanism parameters. Our models are intended as a step towards more complex and realistic modelling work. Future studies should include additional components such as magma compressibility, reservoir poroelasticity, and crustal viscoelasticity that could further influence the system's evolution over time.

Acknowledgments

No datasets were generated or analysed during the current study. Rami Alshembari is grateful to the University of Exeter for funding his PhD studentship. We thank Mathew Head for useful discussions and comments in the early stages of this work.

Author Statement

Rami Alshembari: Conceptualization, Methodology, Software, Writing - Original Draft, Visualization, Formal analysis
James Hickey: Validation, Software, Supervision, Writing - Review & Editing.

Ben J. Williamson and Katharine Cashman: Writing - Review & Editing.

References:

Amoruso, A., & Crescentini, L. (2009). Shape and volume change of pressurized ellipsoidal cavities from deformation and seismic data. *Journal of Geophysical Research*, *114*(B2), B02210. https://doi.org/10.1029/2008JB005946

Anderson, A. T. (1976). Magma mixing: petrological process and volcanological tool. *Journal of Volcanology and Geothermal Research*, *1*(1), 3–33. https://doi.org/10.1016/0377-0273(76)90016-0

Anderson, K., & Segall, P. (2011). Physics-based models of ground deformation and extrusion rate at effusively erupting volcanoes. *Journal of Geophysical Research*, *116*(B7), B07204. https://doi.org/10.1029/2010JB007939

Annen, C., Blundy, J. D., Leuthold, J., & Sparks, R. S. J. (2015). Lithos Construction and evolution of igneous bodies : Towards an integrated perspective of crustal magmatism. *LITHOS*, *230*, 206–221. https://doi.org/10.1016/j.lithos.2015.05.008

Aravena, Á., Cioni, R., de'Michieli Vitturi, M., & Neri, A. (2018). Conduit stability effects on intensity and steadiness of explosive eruptions. *Scientific Reports*, *8*(1), 4125. https://doi.org/10.1038/s41598-018-22539-8

Bachmann, O., & Huber, C. (2016). Silicic magma reservoirs in the Earth's crust. *American Mineralogist*, *101*(11), 2377–2404. https://doi.org/10.2138/am-2016-5675

Bato, M. G., Pinel, V., Yan, Y., Jouanne, F., & Vandemeulebrouck, J. (2018). Possible deep

connection between volcanic systems evidenced by sequential assimilation of geodetic data. *Scientific Reports*, *8*(1), 11702. https://doi.org/10.1038/s41598-018-29811-x

Biggs, J., Ebmeier, S. K., Aspinall, W. P., Lu, Z., Pritchard, M. E., Sparks, R. S. J., & Mather, T. A. (2014). Global link between deformation and volcanic eruption quantified by satellite imagery. *Nature Communications*, *5*(1), 3471. https://doi.org/10.1038/ncomms4471

Bonafede, M., Dragoni, M., & Quareni, F. (1986). Displacement and stress fields produced by a centre of dilation and by a pressure source in a viscoelastic half-space: application to the study of ground deformation and seismic activity at Campi Flegrei, Italy. *Geophysical Journal International*, *87*(2), 455–485. https://doi.org/10.1111/j.1365-246X.1986.tb06632.x

Caricchi, L., Burlini, L., & Ulmer, P. (2008). Propagation of P and S-waves in magmas with different crystal contents: Insights into the crystallinity of magmatic reservoirs. *Journal of Volcanology and Geothermal Research*, *178*(4), 740–750. https://doi.org/10.1016/j.jvolgeores.2008.09.008

Carmichael, R. S. (2017). *Practical Handbook of Physical Properties of Rocks and Minerals*. CRC Press. https://doi.org/10.1201/9780203710968

Cashman, K. V., Sparks, R. S. J., & Blundy, J. D. (2017). Vertically extensive and unstable magmatic systems: A unified view of igneous processes. *Science*, *355*(6331), eaag3055. https://doi.org/10.1126/science.aag3055

Chang, W.-L., Smith, R. B., Farrell, J., & Puskas, C. M. (2010). An extraordinary episode of Yellowstone caldera uplift, 2004-2010, from GPS and InSAR observations. *Geophysical Research Letters*, *37*(23), n/a-n/a. https://doi.org/10.1029/2010GL045451

Cruden, A. R., & Weinberg, R. F. (2018). Mechanisms of Magma Transport and Storage in the Lower and Middle Crust—Magma Segregation, Ascent and Emplacement. In *Volcanic and Igneous Plumbing Systems* (pp. 13–53). Elsevier. https://doi.org/10.1016/B978-0-12-809749-6.00002-9

Currenti, G., & Williams, C. A. (2014). Numerical modeling of deformation and stress fields around a magma chamber: Constraints on failure conditions and rheology. *Physics of the Earth and Planetary Interiors*, *226*, 14–27. https://doi.org/10.1016/j.pepi.2013.11.003

Davis, P. M. (1986). Surface deformation due to inflation of an arbitrarily oriented triaxial

ellipsoidal cavity in an elastic half-space, with reference to Kilauea volcano, Hawaii. *Journal of Geophysical Research: Solid Earth*, *91*(B7), 7429–7438. https://doi.org/10.1029/JB091iB07p07429

Delaney, P. T., & McTigue, D. F. (1994). Volume of magma accumulation or withdrawal estimated from surface uplift or subsidence, with application to the 1960 collapse of Kilauea volcano. *Bulletin of Volcanology*, *56*(6–7), 417–424. https://doi.org/10.1007/BF00302823

DePaolo, D. J. (1981). Trace element and isotopic effects of combined wallrock assimilation and fractional crystallization. *Earth and Planetary Science Letters*, *53*(2), 189–202. https://doi.org/10.1016/0012-821X(81)90153-9

Dragoni, M., & Magnanensi, C. (1989). Displacement and stress produced by a pressurized, spherical magma chamber, surrounded by a viscoelastic shell. *Physics of the Earth and Planetary Interiors*, *56*(3–4), 316–328. https://doi.org/10.1016/0031-9201(89)90166-0

Dragoni, M., & Piombo, A. (2020). A Model for the Effusion Rate Produced by a Magma Pulse. *Geophysical Research Letters*, *47*(5), 1–10. https://doi.org/10.1029/2019GL086193

Dvorak, J. J., & Okamura, A. T. (1987). A hydraulic model to explain variations in summit tilt rate at Kilauea and Mauna Loa Volcanoes (Hawaii). *US Geological Survey Professional Paper*.

Dzurisin, D. (2006). *Volcano Deformation*. Berlin, Heidelberg: Springer Berlin Heidelberg. https://doi.org/10.1007/978-3-540-49302-0

Dzurisin, D., Lisowski, M., & Wicks, C. W. (2009). Continuing inflation at Three Sisters volcanic center, central Oregon Cascade Range, USA, from GPS, leveling, and InSAR observations. *Bulletin of Volcanology*, *71*(10), 1091–1110. https://doi.org/10.1007/s00445-009-0296-4

Edmonds, M., Cashman, K. V., Holness, M., & Jackson, M. (2019). Architecture and dynamics of magma reservoirs. *Philosophical Transactions of the Royal Society A: Mathematical, Physical and Engineering Sciences*, *377*(2139), 20180298. https://doi.org/10.1098/rsta.2018.0298

Fialko, Y., Khazan, Y., & Simons, M. (2001). Deformation due to a pressurized horizontal circular crack in an elastic half-space, with applications to volcano geodesy. *Geophysical*

Journal International, *146*(1), 181–190. https://doi.org/10.1046/j.1365-246X.2001.00452.x

Gerbault, M., Hassani, R., Novoa Lizama, C., & Souche, A. (2018). Three-Dimensional Failure Patterns Around an Inflating Magmatic Chamber. *Geochemistry, Geophysics, Geosystems*, *19*(3), 749–771. https://doi.org/10.1002/2017GC007174

Got, J.-L., Carrier, A., Marsan, D., Jouanne, F., Vogfjörd, K., & Villemin, T. (2017). An analysis of the nonlinear magma-edifice coupling at Grimsvötn volcano (Iceland). *Journal of Geophysical Research: Solid Earth*, *122*(2), 826–843. https://doi.org/10.1002/2016JB012905

Gottsmann, J., Blundy, J., Henderson, S., Pritchard, M. E., & Sparks, R. S. J. (2017). Thermomechanical modeling of the Altiplano-Puna deformation anomaly: Multiparameter insights into magma mush reorganization. *Geosphere*, *13*(4), GES01420.1. https://doi.org/10.1130/GES01420.1

Gudmundsson, A. (2020). *Volcanotectonics*. *Volcanotectonics*. Cambridge University Press. https://doi.org/10.1017/9781139176217

Hammond, J. O. S., Kendall, J.-M., Stuart, G. W., Keir, D., Ebinger, C., Ayele, A., & Belachew, M. (2011). The nature of the crust beneath the Afar triple junction: Evidence from receiver functions. *Geochemistry, Geophysics, Geosystems*, *12*(12), n/a-n/a. https://doi.org/10.1029/2011GC003738

Hautmann, S., Gottsmann, J., Sparks, R. S. J., Mattioli, G. S., Sacks, I. S., & Strutt, M. H. (2010). Effect of mechanical heterogeneity in arc crust on volcano deformation with application to Soufriere Hills Volcano, Montserrat, West Indies. *Journal of Geophysical Research: Solid Earth*, *115*(9), 1–18. https://doi.org/10.1029/2009JB006909

Head, M., Hickey, J., Gottsmann, J., & Fournier, N. (2019). The Influence of Viscoelastic Crustal Rheologies on Volcanic Ground Deformation: Insights From Models of Pressure and Volume Change. *Journal of Geophysical Research: Solid Earth*, *124*(8), 8127–8146. https://doi.org/10.1029/2019JB017832

Head, M., Hickey, J., Gottsmann, J., & Fournier, N. (2021). Exploring the Impact of Thermally Controlled Crustal Viscosity on Volcanic Ground Deformation. *Journal of Geophysical Research: Solid Earth*, *126*(8), 1–22. https://doi.org/10.1029/2020JB020724

Hickey, J., & Gottsmann, J. (2014). Benchmarking and developing numerical Finite Element models of volcanic deformation. *Journal of Volcanology and Geothermal Research*, *280*(June), 126–130. https://doi.org/10.1016/j.jvolgeores.2014.05.011

Hickey, J., Gottsmann, J., & del Potro, R. (2013). The large-scale surface uplift in the Altiplano-Puna region of Bolivia: A parametric study of source characteristics and crustal rheology using finite element analysis. *Geochemistry, Geophysics, Geosystems*, *14*(3), 540–555. https://doi.org/10.1002/ggge.20057

Hickey, J., Gottsmann, J., Nakamichi, H., & Iguchi, M. (2016). Thermomechanical controls on magma supply and volcanic deformation: application to Aira caldera, Japan. *Scientific Reports*, *6*(1), 32691. https://doi.org/10.1038/srep32691

Huppert, H. E., & Woods, A. W. (2002). The role of volatiles in magma chamber dynamics. *Nature*, *420*(6915), 493–495. https://doi.org/10.1038/nature01211

Jackson, M. D., Blundy, J., & Sparks, R. S. J. (2018). Chemical differentiation, cold storage and remobilization of magma in the Earth's crust. *Nature*, *564*(7736), 405–409. https://doi.org/10.1038/s41586-018-0746-2

Jaupart, C., & Tait, S. (1990). Dynamics of eruptive phenomena. *Reviews in Mineralogy*, *24*, 213–238.

Johnson, J. H., Poland, M. P., Anderson, K. R., & Biggs, J. (2019). A Cautionary Tale of Topography and Tilt from Kilauea Caldera. *Geophysical Research Letters*, *46*(8), 4221–4229. https://doi.org/10.1029/2018GL081757

Kilbride, B. M. C., Edmonds, M., & Biggs, J. (2016). Observing eruptions of gas-rich compressible magmas from space. *Nature Communications*, *7*, 1–8. https://doi.org/10.1038/ncomms13744

Kilburn, C. R. J. (2000). Lava flows and flow fields. *Encyclopedia Of Volcanoes*, 291–305.

Lengliné, O., Marsan, D., Got, J.-L., Pinel, V., Ferrazzini, V., & Okubo, P. G. (2008). Seismicity and deformation induced by magma accumulation at three basaltic volcanoes. *Journal of Geophysical Research*, *113*(B12), B12305. https://doi.org/10.1029/2008JB005937

Liao, Y., Soule, S. A., & Jones, M. (2018). On the Mechanical Effects of Poroelastic Crystal

Mush in Classical Magma Chamber Models. *Journal of Geophysical Research: Solid Earth*, *123*(11), 9376–9406. https://doi.org/10.1029/2018JB015985

Lipman, P. W., & Bachmann, O. (2015). Ignimbrites to batholiths: Integrating perspectives from geological, geophysical, and geochronological data. *Geosphere*, *11*(3), 705–743. https://doi.org/10.1130/GES01091.1

MacKenzie, L., Abers, G. A., Fischer, K. M., Syracuse, E. M., Protti, J. M., Gonzalez, V., & Strauch, W. (2008). Crustal structure along the southern Central American volcanic front. *Geochemistry, Geophysics, Geosystems*, *9*(8), n/a-n/a. https://doi.org/10.1029/2008GC001991

Marsh, B. D. (1981). On the crystallinity, probability of occurrence, and rheology of lava and magma. *Contributions to Mineralogy and Petrology*, *78*(1), 85–98. https://doi.org/10.1007/BF00371146

Massol, H., Jaupart, C., & Pepper, D. W. (2001). Ascent and decompression of viscous vesicular magma in a volcanic conduit. *Journal of Geophysical Research: Solid Earth*, *106*(B8), 16223–16240. https://doi.org/10.1029/2001JB000385

Masterlark, T. (2007). Magma intrusion and deformation predictions: Sensitivities to the Mogi assumptions. *Journal of Geophysical Research: Solid Earth*, *112*(6), 1–17. https://doi.org/10.1029/2006JB004860

McTigue, D. F. (1987). Elastic stress and deformation near a finite spherical magma body: Resolution of the point source paradox. *Journal of Geophysical Research*, *92*(B12), 12931. https://doi.org/10.1029/JB092iB12p12931

Mével, H. Le, Feigl, K. L., Cõrdova, L., DeMets, C., & Lundgren, P. (2015). Evolution of unrest at Laguna del Maule volcanic field (Chile) from InSAR and GPS measurements, 2003 to 2014. *Geophysical Research Letters*, *42*(16), 6590–6598. https://doi.org/10.1002/2015GL064665

Le Mével, H., Gregg, P. M., & Feigl, K. L. (2016). Magma injection into a long-lived reservoir to explain geodetically measured uplift: Application to the 2007-2014 unrest episode at Laguna del Maule volcanic field, Chile. *Journal of Geophysical Research: Solid Earth*, *121*(8), 6092–6108. https://doi.org/10.1002/2016JB013066

Mogi, K. (1958). Relation between the eruptions of various volcanoes and the deformations of the ground surface around them. *Bull. Earthq. Res. Inst., Univ. Tokyo*, *38*, 99–134. Retrieved from http://ci.nii.ac.jp/naid/10019750786/en/

Morales Rivera, A. M., Amelung, F., & Mothes, P. (2016). Volcano deformation survey over the Northern and Central Andes with ALOS InSAR time series. *Geochemistry, Geophysics, Geosystems*, *17*(7), 2869–2883. https://doi.org/10.1002/2016GC006393

Mutch, E. J. F., Maclennan, J., Shorttle, O., Edmonds, M., & Rudge, J. F. (2019). Rapid transcrustal magma movement under Iceland. *Nature Geoscience*, *12*(7), 569–574. https://doi.org/10.1038/s41561-019-0376-9

Del Negro, C., Currenti, G., & Scandura, D. (2009). Temperature dependent viscoelastic modeling of ground deformation: Application to Etna volcano during the 1993–1997 inflation period. *Physics of the Earth and Planetary Interiors*, *172*(3–4), 299–309. https://doi.org/10.1016/j.pepi.2008.10.019

Nooner, S. L., & Chadwick, W. W. (2009). Volcanic inflation measured in the caldera of axial seamount: Implications for magma supply and future eruptions. *Geochemistry, Geophysics, Geosystems*, *10*(2). https://doi.org/10.1029/2008GC002315

Palacios, J., & Armstrong, H. L. (1965). Dimensional Analysis. *American Journal of Physics*, *33*(6), 513–514. https://doi.org/10.1119/1.1971812

Pascal, K., Neuberg, J., & Rivalta, E. (2014). On precisely modelling surface deformation due to interacting magma chambers and dykes. *Geophysical Journal International*, *196*(1), 253–278. https://doi.org/10.1093/gji/ggt343

Phillipson, G., Sobradelo, R., & Gottsmann, J. (2013). Global volcanic unrest in the 21st century: An analysis of the first decade. *Journal of Volcanology and Geothermal Research*, *264*, 183–196. https://doi.org/10.1016/j.jvolgeores.2013.08.004

Reverso, T., Vandemeulebrouck, J., Jouanne, F., Pinel, V., Villemin, T., Sturkell, E., & Bascou, P. (2014). A two-magma chamber model as a source of deformation at Grímsvötn Volcano, Iceland. *Journal of Geophysical Research: Solid Earth*, *119*(6), 4666–4683. https://doi.org/10.1002/2013JB010569

Rosenberg, C. L., & Handy, M. R. (2005). Experimental deformation of partially melted granite

revisited: Implications for the continental crust. *Journal of Metamorphic Geology*, *23*(1), 19–28. https://doi.org/10.1111/j.1525-1314.2005.00555.x

Segall, P. (2013). Volcano deformation and eruption forecasting. *Geological Society, London, Special Publications*, *380*(1), 85–106. https://doi.org/10.1144/SP380.4

Segall, P. (2016). Repressurization following eruption from a magma chamber with a viscoelastic aureole. *Journal of Geophysical Research: Solid Earth*, *121*(12), 8501–8522. https://doi.org/10.1002/2016JB013597

Segall, P. (2019). Magma chambers: what we can, and cannot, learn from volcano geodesy. *Philosophical Transactions of the Royal Society A: Mathematical, Physical and Engineering Sciences*, *377*(2139), 20180158. https://doi.org/10.1098/rsta.2018.0158

Sparks, R. S. J., Biggs, J., & Neuberg, J. W. (2012). Monitoring volcanoes. *Science*, *335*(6074), 1310–1311. https://doi.org/10.1126/science.1219485

Sparks, R. S. J., Annen, C., Blundy, J. D., Cashman, K. V., Rust, A. C., & Jackson, M. D. (2019). Formation and dynamics of magma reservoirs. *Philosophical Transactions of the Royal Society A: Mathematical, Physical and Engineering Sciences*, *377*(2139), 20180019. https://doi.org/10.1098/rsta.2018.0019

Suhardja, S. K., Widiyantoro, S., Métaxian, J.-P., Rawlinson, N., Ramdhan, M., & Budi-Santoso, A. (2020). Crustal thickness beneath Mt. Merapi and Mt. Merbabu, Central Java, Indonesia, inferred from receiver function analysis. *Physics of the Earth and Planetary Interiors*, *302*(February), 106455. https://doi.org/10.1016/j.pepi.2020.106455

Trasatti, E., Bonafede, M., Ferrari, C., Giunchi, C., & Berrino, G. (2011). On deformation sources in volcanic areas: Modeling the Campi Flegrei (Italy) 1982–84 unrest. *Earth and Planetary Science Letters*, *306*(3–4), 175–185. https://doi.org/10.1016/j.epsl.2011.03.033

Turcotte, D., & Schubert, G. (2014). *Geodynamics, 3rd edition* (Vol. 40). Retrieved from http://doi.wiley.com/10.1002/1521-3773(20010316)40:6%3C9823::AID-ANIE9823%3E3.3.CO;2-C

Yang, X.-M., Davis, P. M., & Dieterich, J. H. (1988). Deformation from inflation of a dipping finite prolate spheroid in an elastic half-space as a model for volcanic stressing. *Journal of Geophysical Research: Solid Earth*, *93*(B5), 4249–4257.

https://doi.org/10.1029/JB093iB05p04249

Highlights

- Two magma intrusion schemes are compared, examining the magma reservoir pressure evolution through time and resultant surface deformation
- Reservoir pressurization is influenced by characteristic timescales related to the dimensions of the feeder system and magma rheology